




# Novel yolk–shell Fe<sub>3</sub>O<sub>4</sub>@void@SiO<sub>2</sub>@PPy nanochains toward microwave absorption application

Mingtao Qiao<sup>1,2,\*</sup> , Dan Wei<sup>2</sup>, Xiaowei He<sup>2</sup>, Xingfeng Lei<sup>2</sup>, Jian Wei<sup>1</sup>, and Qiuyu Zhang<sup>2,3,\*</sup>

<sup>1</sup> College of Materials Science and Engineering, Shaanxi Key Laboratory of Nano-materials and Technology, Xi'an University of Architecture and Technology, Xi'an 710055, Shaanxi, People's Republic of China

<sup>2</sup> School of Chemistry and Chemical Engineering, Northwestern Polytechnical University, Xi'an 710072, People's Republic of China

<sup>3</sup> MOE Key Laboratory of Material Physics and Chemistry Under Extraordinary Condition, Ministry of Education, Northwestern Polytechnical University, Xi'an 710072, People's Republic of China

Received: 13 May 2020

Accepted: 8 September 2020

Published online:  
18 September 2020

© Springer Science+Business  
Media, LLC, part of Springer  
Nature 2020

## ABSTRACT

A growing number of core–shell structured microwave absorbents have been reported; nevertheless, there are few studies accessible about one-dimensional core–shell electromagnetic nanocomposites as microwave absorption materials. In this work, we have developed two kinds of novel electromagnetic nanocomposites, namely yolk–shell Fe<sub>3</sub>O<sub>4</sub>@void@SiO<sub>2</sub> nanochains and Fe<sub>3</sub>O<sub>4</sub>@void@SiO<sub>2</sub>@PPy nanochains. Their components and morphologies have been characterized by X-ray diffraction (XRD), X-ray photoelectron spectra, scanning electron microscope and transmission electron microscope. The N<sub>2</sub> adsorption–desorption isotherms have demonstrated their specific surface areas and porosity, and the magnetic properties have been recorded by the vibrating sample magnetometer. Investigation of microwave absorbing properties manifests that Fe<sub>3</sub>O<sub>4</sub>@void@SiO<sub>2</sub>@PPy nanochains have stronger absorption capability and broader effective absorption bandwidth than Fe<sub>3</sub>O<sub>4</sub>@void@SiO<sub>2</sub> nanochains, which is caused by the introduction of polypyrrole shells, giving rise to the addition of conductive loss and the enhancement of dipole polarizations, interfacial polarizations, multiple reflection and absorption. Specifically, the minimum reflection loss value is – 54.2 dB (17.70 GHz) and the maximum effective absorption bandwidth can reach 5.90 GHz (11.49–17.39 GHz); thus, Fe<sub>3</sub>O<sub>4</sub>@void@SiO<sub>2</sub>@PPy nanochains will become promising microwave absorption candidates. This research once more demonstrates that necklace-like core–shell magnetic–dielectric complex benefit to enhancement of microwave absorption performance, and establishes a good foundation for exploiting the high-effective microwave absorbing materials.

Handling Editor: Dale Huber.

Address correspondence to E-mail: mtqiao@xauat.edu.cn; qyzzhang@nwpu.edu.cn

## Introduction

Over the past five years, lots of new and smart electronic devices have been emerging around us, because they can facilitate people's livelihood and improve the work efficiency. Indeed, all of electronic devices are carriers of frequency-dependent electromagnetic waves. Produced electromagnetic radiation is an invisible hazard, which not only threatens the human health directly but also interferes the surrounded devices [1–3]. Human beings become aware of the seriousness of electromagnetic pollution gradually, and even call it as the fourth largest pollution in the environment. Now, to solve the electromagnetic pollution is necessary and urgent. Exploitation of microwave absorption materials has been regarded as an effective and important approach to preventing electromagnetic radiation. That is because microwave absorption materials are able to convert incident electromagnetic energy to thermal energy or other energies, reducing the harm and building a friendly environment [4, 5].

It is well known that ideal microwave absorption materials need to meet three major advantages of large absorption intensity, wide absorption frequency band and lightweight. Up to now, numerous absorbers with strong reflection loss performance have been successfully developed, but it is still difficult to broaden the absorption bandwidth. According to the microwave absorption mechanisms, absorption bandwidth is mainly attributed to impedance matching and multiple losses [6, 7]. To improve impedance matching degree and enhance attenuation capacity, the conjugation of magnetic materials and dielectric materials has attracted considerable attentions. Rational construction of magnetic–dielectric materials can not only bring the strong magnetic loss and dielectric loss but also narrow the gap between permeability and permittivity, reaching a relatively high impedance matching degree. Particularly, core–shell-type magnetic–dielectric materials have exhibited huge potentials in the microwave absorption application, such as CoNi@SiO<sub>2</sub>@TiO<sub>2</sub> microspheres [8], Co<sub>20</sub>Ni<sub>80</sub>@TiO<sub>2</sub> particles [9], Fe<sub>3</sub>O<sub>4</sub>@SnO<sub>2</sub> nanorods [10], Fe<sub>3</sub>O<sub>4</sub>@C microspheres [11], Fe<sub>3</sub>O<sub>4</sub>@TiO<sub>2</sub> microspheres [12], Ni@SnO<sub>2</sub> hybrid [13], Ni@TiO<sub>2</sub> and Ni@SiO<sub>2</sub> microspheres [14], Co@C microspheres [15], Fe<sub>3</sub>O<sub>4</sub>@PEDOT microspheres [16] and ZnFe<sub>2</sub>O<sub>4</sub>@SiO<sub>2</sub>@RGO microspheres [17]. Moreover, a

special core@void@shell configuration, named yolk–shell structure, is endowed with several special advantages, such as low density, large surface area and interstitial void space. These tunable characterizations benefit to optimizing the electromagnetic parameters and further improving microwave absorption performance.

Recently, one-dimensional (1D) structured electromagnetic materials have attracted increasing interest in field of microwave absorption owing to the high surface-to-volume ratio and the isotropic antenna dissipation mechanism, such as Fe<sub>3</sub>O<sub>4</sub>/carbon nanotubes, Fe/SiC hybrid fibers, Fe<sub>3</sub>O<sub>4</sub>/Fe nanowires and FeCo nanochains [18–21]. Additionally, they are 1D materials that can exhibit superior microwave absorption properties than the bulk and particle forms due to their network-like structures in the composites [22–24]. However, there exists a common defect among the previously reported 1D nanocomposites. Their magnetic components are exposed to the outside, which easily suffer from oxidation or corrosion. Through the design of core–shell structure, stable dielectric shells, such as SiO<sub>2</sub>, carbon materials and conducting polymers, can protect the magnetic cores absolutely. Thus, 1D structured nanocomposites together with magnetic materials as cores and SiO<sub>2</sub>/carbon/conducting polymer materials as shells are expected in the practical application of microwave absorption.

Interestingly, in our previous work, as-synthesized yolk–shell Fe<sub>3</sub>O<sub>4</sub>@N-doped carbon nanochains possess the minimum reflection loss value of – 63.09 dB (11.91 GHz) and broad effective frequency bandwidth of 5.7 GHz (11.11–16.81 GHz), exhibiting highly effective microwave absorption performance [25]. Furthermore, Fe<sub>3</sub>O<sub>4</sub>@SiO<sub>2</sub>@MnO<sub>2</sub> nanochains have the maximum effective absorption frequency bandwidth of 5.28 GHz (10.15–15.43 GHz) [26]. These results indicate the superiority of core–shell magnetic–dielectric nanochains in the improvement of effective absorption frequency bandwidth. It is known that MnO<sub>2</sub> shells are subject to acid environment; moreover, they have weak interfacial interaction with the polymer matrix, affecting the microwave absorption efficiency and reducing the mechanical properties. Actually, polypyrrole (PPy) has been deemed to more appropriate outer shells than metal oxides (e.g., NiO, MnO, ZnO) in the core–shell magnetic–dielectric nanochains, owing to good chemical stability, intrinsic lightweight feature,

tunable dielectric properties and outstanding interfacial compatibility [27]. However, there are few related studies accessible yet.

Herein, we have synthesized two kinds of core-shell nanochains, namely  $\text{Fe}_3\text{O}_4@\text{void@SiO}_2$  and  $\text{Fe}_3\text{O}_4@\text{void@SiO}_2@\text{PPy}$ . As we all know,  $\text{SiO}_2$  is a common wave-transparent material. So  $\text{Fe}_3\text{O}_4@\text{void@SiO}_2$  nanochains possess the minimum reflection loss value of  $-24.7$  dB (17.34 GHz). With the addition of PPy shells, microwave absorption performance has been improved a lot. The absorption peak is  $-54.20$  dB (17.7 GHz), and the effective absorption bandwidth ranges from 11.49 GHz to 17.39 GHz. It can be seen that PPy shells can enhance the microwave absorption performance of yolk-shell  $\text{Fe}_3\text{O}_4@\text{void@SiO}_2$  nanochains. Eventually, the detailed microwave absorption mechanism has been investigated.

## Experimental section

### Synthesis of yolk-shell $\text{Fe}_3\text{O}_4@\text{void@SiO}_2$ and $\text{Fe}_3\text{O}_4@\text{void@SiO}_2@\text{PPy}$ nanochains

All chemicals were of analytical grade and used as received without any further purification. Based on our previous reports, porous  $\text{Fe}_3\text{O}_4$  magnetic particles as “building blocks” and  $\text{Fe}_3\text{O}_4@\text{P}(\text{DVB-MAA})$  nanochains were prepared via modified hydrothermal method and magnetic-field-induced precipitation polymerization [28–30]. Then, a simple sol-gel method was applied to grow the  $\text{SiO}_2$  shells on the surface of  $\text{Fe}_3\text{O}_4@\text{P}(\text{DVB-MAA})$  nanochains. Typically, 0.03 g of  $\text{Fe}_3\text{O}_4@\text{P}(\text{DVB-MAA})$  nanochains was dispersed in a mixed solvent including 80 mL ethanol, 8 mL DI water and 2 mL ammonia. This mixture was transferred into a three-necked flask; after mechanically stirring for an hour, 100  $\mu\text{L}$  TEOS was injected into the above mixture. The reaction was proceeding for 10 h at room temperature. The products were separated, washed several times with ethanol and deionized water and vacuum-dried at 80 °C overnight. The core-double-shell  $\text{Fe}_3\text{O}_4@\text{P}(\text{MAA-DVB})@\text{SiO}_2$  nanochains were obtained. Subsequently, these nanochains were heated from room temperature to 600 °C at a heating rate of 1 °C/min and sintered at 600 °C for 6 h under the flowing argon. The final products are yolk-shell  $\text{Fe}_3\text{O}_4@\text{void@SiO}_2$  nanochains. Then, with the guidance of

our previous work [31], the chemical oxidative polymerization was applied to make polypyrrole successfully grow on the surface of  $\text{Fe}_3\text{O}_4@\text{void@SiO}_2$  nanochains in the presence of PVA and *p*-toluenesulfonic acid. Briefly, 0.02 g of  $\text{Fe}_3\text{O}_4@\text{void@SiO}_2$  nanochains was well dispersed in the PVA (1 wt %, 80 mL) aqueous solution. The above mixture was transferred into a three-necked flask; meanwhile, both *p*-TSA (3.0 g) and pyrrole monomers (0.2 g) were added. Through the mechanical agitation for several hours in an ice-water bath, the system temperature keeps 0–5 °C. The ammonium persulfate solution (10 mL, 0.68 g) was added dropwise into the above mixture. After the polymerization reaction for six hours, the products were collected through magnetic separation, washed several times with ethanol and deionized water and dried under vacuum at 80 °C overnight. The yolk-shell  $\text{Fe}_3\text{O}_4@\text{void@SiO}_2@\text{PPy}$  nanochains were obtained.

## Characterization

The GSL-1700X tube furnace was employed to calcine the samples. Fourier transform infrared (FTIR) spectra in the range of 400–4000  $\text{cm}^{-1}$  were recorded on KBr powder-pressed pellets with a Bruker Tensor 27 spectrometer. X-ray diffraction patterns (XRD) were obtained via the Shimadzu XRD-7000 s diffractometer with  $\text{Cu K}\alpha$  radiation ( $\lambda = 1.542 \text{ \AA}$ ) from 20° to 80°. The morphologies of samples were observed by a field emission scanning electron microscope (FE-SEM, ZEISS EVO 18 Research) with an accelerating voltage of 15 kV. The detailed microstructure was revealed by the transmission electron microscope (TEM) performed on the JEOL JEM-2010 transmission electron microscope with an accelerating voltage of 200 kV. The  $\text{N}_2$  adsorption/desorption isotherms were recorded on a TriStar II 20 apparatus, and the specific surface area and pore volume analysis were performed by Brunauer–Emmett–Teller (BET) and Barrett–Joyner–Halenda (BJH) methods, respectively. The magnetic properties of products were assessed using a vibrating sample magnetometer (VSM, LakeShore 7307) at room temperature. The microwave absorption measurements of samples were carried out by a vector network analyzer (VNA, Agilent N5227) equipped with a coaxial transmission waveguide in the frequency range of 2–18 GHz. Prior to measurement, the mixture of samples and wax at specific mass ratio was pressed into an appropriate

toroidal-shaped sample ( $\Phi_{\text{outer}} = 7.00$  mm and  $\Phi_{\text{inner}} = 3.04$  mm). Then, the electromagnetic parameters including  $\epsilon', \epsilon'', \mu', \mu''$  were recorded on a standard HP software module 85071E at room temperature. Finally, the reflection loss (RL) values of samples with different layer thicknesses can be calculated on the basis of the following formulas:

$$Z_{\text{in}} = Z_0 \sqrt{\mu_r / \epsilon_r} \tanh [j(2\pi f d / c) \sqrt{\mu_r \epsilon_r}] \quad (1)$$

$$\text{RL}(\text{dB}) = 20 \log |(Z_{\text{in}} - Z_0) / (Z_{\text{in}} + Z_0)| \quad (2)$$

where  $Z_0$  represents the impedance of free space,  $Z_{\text{in}}$  is the normalized input impedance of a metal-backed microwave absorption layer,  $f$  is the frequency of electromagnetic wave,  $c$  is the velocity of light in free space,  $d$  is the layer thickness and the RL is the reflection loss value. The relative complex permittivity ( $\epsilon_r$ ) and relative complex permeability ( $\mu_r$ ) of the absorbing medium are expressed as  $\epsilon_r = \epsilon' - j\epsilon''$  and  $\mu_r = \mu' - j\mu''$ .

### Results and discussion

A detailed synthetic illustration of  $\text{Fe}_3\text{O}_4@$ void@ $\text{SiO}_2@$ PPy nanochains is shown in Fig. 1. During the past several years, our group has prepared a series of necklace-like magnetic nanochains through magnetic-field-induced distillation–precipitation polymerization, and their formation mechanism has been described in some important studies [25, 29, 30]. Here, we can easily prepare the  $\text{Fe}_3\text{O}_4@$ P(DVB-MAA) nanochains. Then, modified “Stöber” method is utilized to prepare the core–double-shell  $\text{Fe}_3\text{O}_4@$ P(DVB-MAA)@ $\text{SiO}_2$  nanochains. Owing to lots of carboxylic acid groups on the surface, as-obtained

$\text{Fe}_3\text{O}_4@$ P(DVB-MAA) nanochains have good dispersion in the mixed solvents of water and ethanol. Moreover, these carboxylic acid groups can facilitate the growth of  $\text{SiO}_2$  shells [32]. When  $\text{Fe}_3\text{O}_4@$ P(DVB-MAA)@ $\text{SiO}_2$  nanochains are calcined at 600 °C for 6 h, the polymer P(DVB-MAA) shells can be removed completely, leading to the formation of yolk–shell  $\text{Fe}_3\text{O}_4@$ void@ $\text{SiO}_2$  nanochains. Additionally, enlightened by our previous work, we also make the polypyrrole (PPy) shells encapsulate the  $\text{Fe}_3\text{O}_4@$ void@ $\text{SiO}_2$  nanochains through the chemical oxidative polymerization in the presence of poly(vinyl alcohol) and p-toluenesulfonic acid [31]. The yolk–shell  $\text{Fe}_3\text{O}_4@$ void@ $\text{SiO}_2@$ PPy nanochains are also prepared successfully.

Figure 2 depicts the morphologies of  $\text{Fe}_3\text{O}_4@$ P(DVB-MAA) and  $\text{Fe}_3\text{O}_4@$ P(DVB-MAA)@ $\text{SiO}_2$  nanochains. From the SEM images in Fig. 2a and c, lots of straight nanochains can be observed. According to the histogram of chain length distribution shown in Figure S1, the chain length of  $\text{Fe}_3\text{O}_4@$ P(DVB-MAA) nanochains mainly distributes in the range of 10–24  $\mu\text{m}$ , and that of someone can exceed 30  $\mu\text{m}$ . But the chain length of  $\text{Fe}_3\text{O}_4@$ P(DVB-MAA)@ $\text{SiO}_2$  nanochains is 8–18  $\mu\text{m}$ , less than that of  $\text{Fe}_3\text{O}_4@$ P(DVB-MAA) nanochains. This may be originated from the strong mechanically stirring, leading to interruption of some chains. The TEM images not only exhibit the necklace-like morphology but also reveal the core–shell structure of nanochains. As shown in Fig. 2b and d, the thickness of P(DVB-MAA) shells is ca. 20 nm and that of  $\text{SiO}_2$  shell is ca. 50 nm. And the space between the magnetic spheres is 10–12 nm in the single nanochain, which may be related to the external magnetic field intensity. Figure 2e shows the FTIR spectra of  $\text{Fe}_3\text{O}_4$ ,

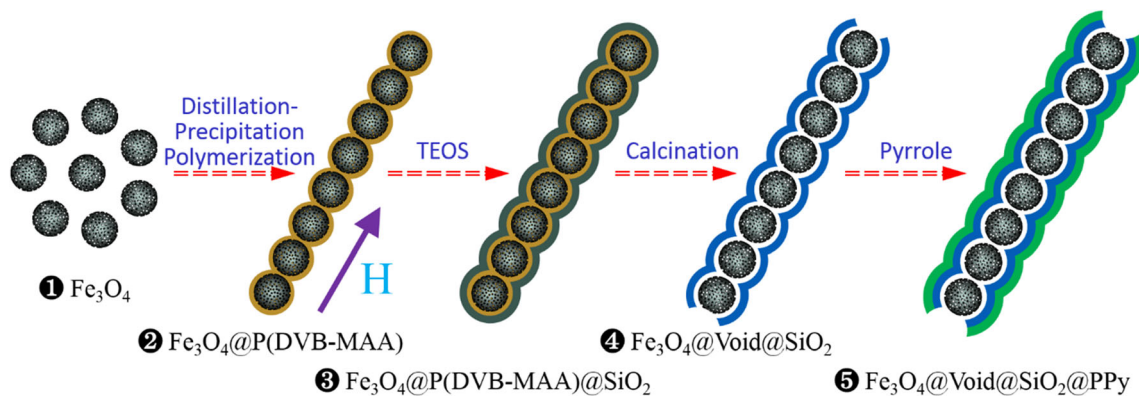
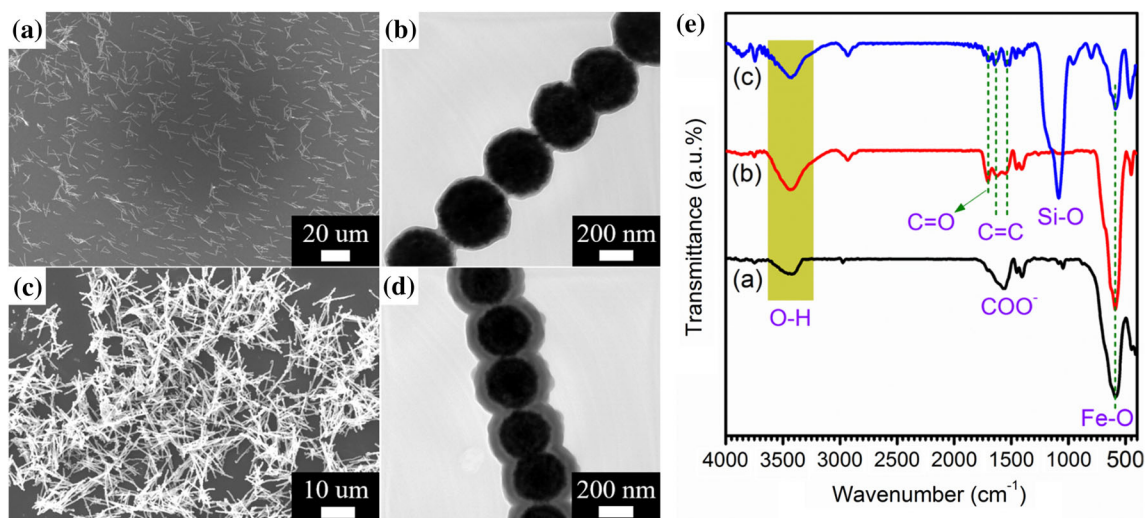


Figure 1 Schematic illustration of the preparation of  $\text{Fe}_3\text{O}_4@$ void@ $\text{SiO}_2@$ PPy nanochains.



**Figure 2** SEM **a** and TEM **b** images of Fe<sub>3</sub>O<sub>4</sub>@P(DVB-MAA) nanochains and SEM **c** and TEM **d** images of Fe<sub>3</sub>O<sub>4</sub>@P(DVB-MAA)@SiO<sub>2</sub> nanochains. **e** FTIR spectra of samples: **a** Fe<sub>3</sub>O<sub>4</sub>,

**b** Fe<sub>3</sub>O<sub>4</sub>@P(DVB-MAA) and **c** Fe<sub>3</sub>O<sub>4</sub>@P(DVB-MAA)@SiO<sub>2</sub> nanochains.

Fe<sub>3</sub>O<sub>4</sub>@P(DVB-MAA) and Fe<sub>3</sub>O<sub>4</sub>@P(DVB-MAA)@SiO<sub>2</sub> nanochains. The sharp peak at 587 cm<sup>-1</sup> appears in the each curve, which is attributed to Fe–O bonds from the Fe<sub>3</sub>O<sub>4</sub> microspheres. In curve (a), the peak at 1565 cm<sup>-1</sup> corresponds to the asymmetrical stretching vibration of carboxylates such as sodium polymethacrylate and sodium citrate. In curve (b), the absorption peak of C=O group in the PMAA is located at the 1721 cm<sup>-1</sup>. Both of two peaks at 1633 cm<sup>-1</sup> and 1535 cm<sup>-1</sup> indicate the stretching vibration of C=C bonds in the benzene skeleton. Furthermore, the formation of P(DVB-MAA) is verified. In curve (c), the strong peak at 1080 cm<sup>-1</sup> is assigned to the Si–O bonds, demonstrating the growth of SiO<sub>2</sub> shells. In addition, a broad peak at 3200–3600 cm<sup>-1</sup> (green background) is attributed to the stretching vibration of hydroxyl group. The above results indicate the formation of Fe<sub>3</sub>O<sub>4</sub>@P(DVB-MAA) and Fe<sub>3</sub>O<sub>4</sub>@P(DVB-MAA)@SiO<sub>2</sub> nanochains.

Figure 3 shows the morphology of Fe<sub>3</sub>O<sub>4</sub>@void@SiO<sub>2</sub> nanochains. As we can see in Fig. 3a, products still keep the one-dimensional orientation structure and their length has no obvious changes before and after calcination, both of which may be ascribed to the protection of SiO<sub>2</sub> shells. From the histogram in Figure S1, one can find that few chains with smaller length appear, which may be caused by the strong ultrasonic and mechanically stirring. Interestingly, from the magnified SEM image in Fig. 3b, yolk-shell structure can be found in the

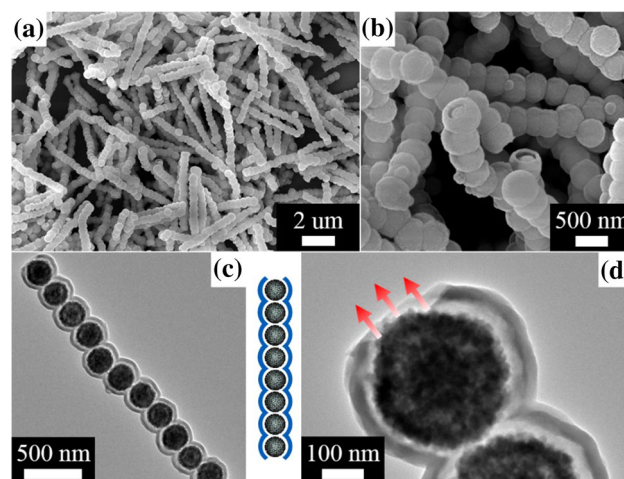


**Figure 3** SEM (**a**, **b**) and TEM (**c**, **d**) images of yolk-shell Fe<sub>3</sub>O<sub>4</sub>@void@SiO<sub>2</sub> nanochains.

head/tail side of nanochains. This architecture has been confirmed again by the TEM images. The formation of voids is caused by the remove of P(DVB-MAA) polymers under the high-temperature pyrolysis, which has also been evidenced by the Yang group [33, 34]. In addition, the magnified TEM images in Fig. 3d demonstrate that some gaseous small molecules (marked with red arrows) have generated and released during the pyrolysis of P(DVB-MAA). Moreover, through the contrast of Figs. 2d and 3c, it can be found that Fe<sub>3</sub>O<sub>4</sub> particles possess more pores after calcination, which may be ascribed to the gasification of PAAs pyrolysis. However, the thickness of

SiO<sub>2</sub> shells also has no change before and after calcination.

From the SEM images in Fig. 4, one can see the surface of nanochains becomes rough, which may be caused by the stack of PPy nanoparticles. Moreover, based on the histogram of chain length distribution in Figure S1, it can be found that the introduction of PPy shells has no effect on chain length of precursors, and both Fe<sub>3</sub>O<sub>4</sub>@void@SiO<sub>2</sub> and Fe<sub>3</sub>O<sub>4</sub>@void@SiO<sub>2</sub>@PPy nanochains are mainly in the range of 8–13 μm. The TEM images show the distinct core–double-shell structure in the nanochains; moreover, the magnified TEM image shows the thickness of PPy shells is ca. 20 nm. Figure 5 exhibits the XRD patterns of Fe<sub>3</sub>O<sub>4</sub>@void@SiO<sub>2</sub> and Fe<sub>3</sub>O<sub>4</sub>@void@SiO<sub>2</sub>@PPy nanochains. It can be found that these two curves have the same diffraction peaks, which very match with the standard PDF card of JCDPS 79-0419. They are, respectively, located 18.2°, 30.0°, 35.6°, 37.2°, 43.2°, 53.5°, 57.2° and 62.8°, corresponding to the (111), (220), (311), (222), (400), (422), (511) and (440) Bragg reflections. This result indicates the crystal form of Fe<sub>3</sub>O<sub>4</sub> is the same as the original ones before calcination [35]. And the broad peaks at 16°–27° are attributed to amorphous SiO<sub>2</sub> and PPy in the two curves. In addition, the XPS spectra can also verify the results. From Fig. 6a, one can see that the N elements appear in the wide scan spectrum of Fe<sub>3</sub>O<sub>4</sub>@void@SiO<sub>2</sub>@PPy nanochains, which mainly originate from the PPy. Moreover, in Fig. 6b, the N 1s core-level spectrum can be deconvoluted two major components of positively charged nitrogen (N<sup>+</sup>) and amine-like (–NH–), corresponding the binding energy of 401.6 eV and 399.8 eV. The peak area ratio

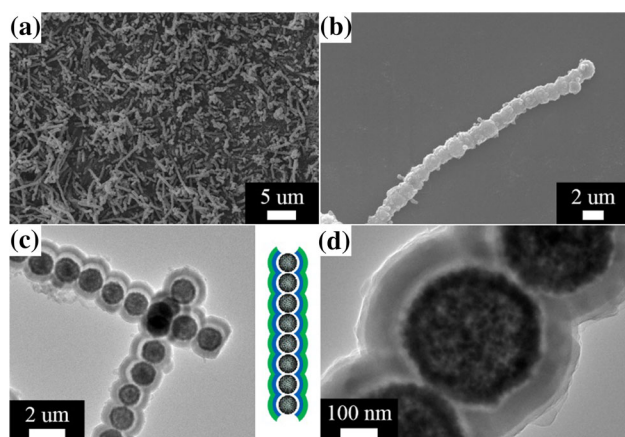


**Figure 4** SEM (a, b) and TEM (c, d) images of yolk–shell Fe<sub>3</sub>O<sub>4</sub>@void@SiO<sub>2</sub>@PPy nanochains.

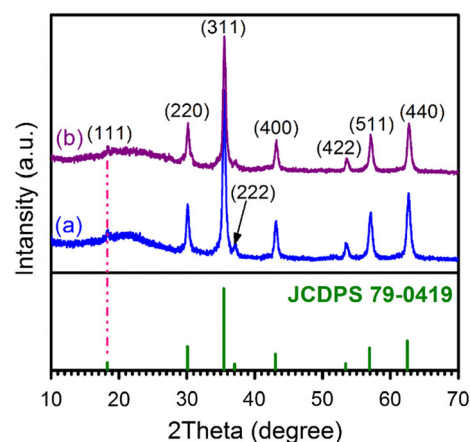


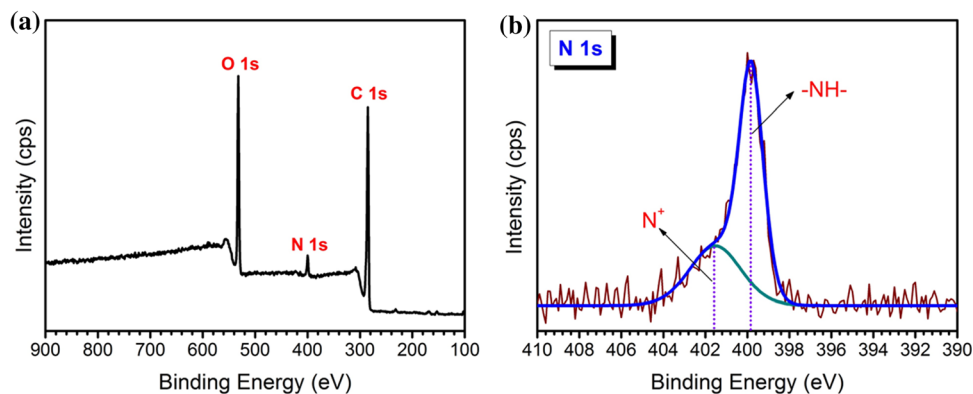
**Figure 5** XRD patterns of a Fe<sub>3</sub>O<sub>4</sub>@void@SiO<sub>2</sub> and b Fe<sub>3</sub>O<sub>4</sub>@void@SiO<sub>2</sub>@PPy nanochains.

of N<sup>+</sup> to N 1 s is about 23.53%, which denotes the doping degree of polypyrrole.

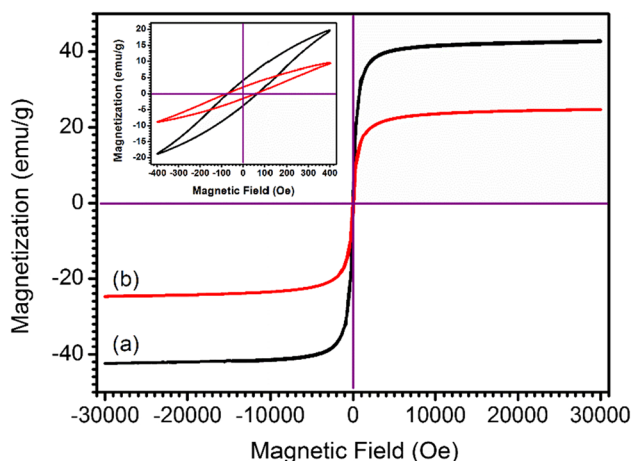
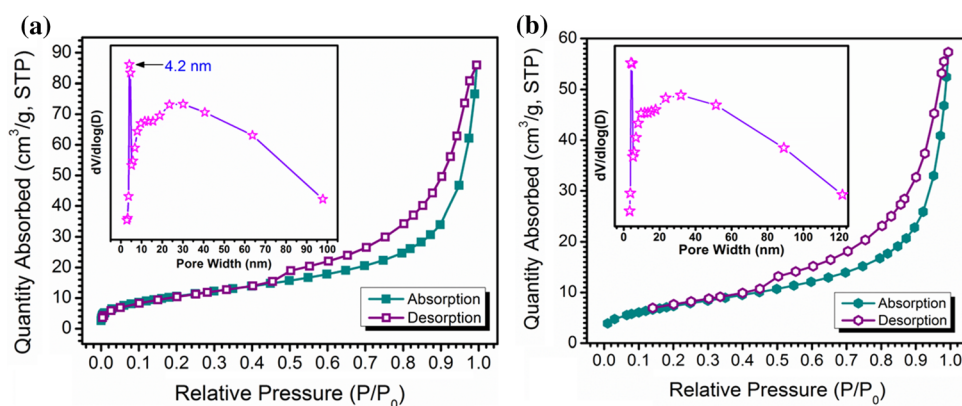
The porosity and specific surface area of samples can be determined by the N<sub>2</sub> absorption–desorption isotherms, which are shown in Fig. 7. It can be found that both of isotherms belong to the IV type and the appearance of H3-type hysteresis loop ( $P/P_0 > 0.4$ ) indicates the existence of pores. Furthermore, the two insets are nearly the same, which demonstrates these two products have the similar pore width distribution. Specifically, the pores with ca. 4.2 nm diameter are the most percentages, which may originate from the Fe<sub>3</sub>O<sub>4</sub> cores, and the pores ranging from 20 to 30 nm are also majority, which are most derived from the voids between cores and shells in the nanochains. After calculation, Fe<sub>3</sub>O<sub>4</sub>@void@SiO<sub>2</sub> nanochains have the BET specific surface area of 49 m<sup>2</sup>/g and BJH pore volume of 0.142 cm<sup>3</sup>/g, whereas, Fe<sub>3</sub>O<sub>4</sub>@void@SiO<sub>2</sub>@PPy nanochains have the BET specific surface area of 42 m<sup>2</sup>/g and BJH pore volume of 0.138 cm<sup>3</sup>/g.

Figure 8 shows the magnetization properties of Fe<sub>3</sub>O<sub>4</sub>@void@SiO<sub>2</sub> and Fe<sub>3</sub>O<sub>4</sub>@void@SiO<sub>2</sub>@PPy nanochains. It can be seen that the specific saturation magnetization ( $M_s$ ) values of Fe<sub>3</sub>O<sub>4</sub>@void@SiO<sub>2</sub> and Fe<sub>3</sub>O<sub>4</sub>@void@SiO<sub>2</sub>@PPy nanochains are approximately 42.3 emu/g and 24.7 emu/g, respectively. Such a decline in the saturation magnetization can be attributed to the addition of non-magnetic PPy shells. However, both of nanochains have the same coactivity of ca. 71.5 Oe, and their remanent magnetisms are 3.9 emu/g and 1.9 emu/g, respectively. The same coactivity may be attributed to the same anisotropy,

**Figure 6** XPS spectra of  $\text{Fe}_3\text{O}_4@\text{void}@\text{SiO}_2@\text{PPy}$  nanochains: **a** wide scan spectrum and **b** N 1 s core-level spectrum.



**Figure 7**  $\text{N}_2$  absorption–desorption isotherms of **a**  $\text{Fe}_3\text{O}_4@\text{void}@\text{SiO}_2$  nanochains and **b**  $\text{Fe}_3\text{O}_4@\text{void}@\text{SiO}_2@\text{PPy}$  nanochains. Insets are the corresponding pore width distribution plots.



**Figure 8** Hysteresis loops of **a**  $\text{Fe}_3\text{O}_4@\text{void}@\text{SiO}_2$  nanochains and **b**  $\text{Fe}_3\text{O}_4@\text{void}@\text{SiO}_2@\text{PPy}$  nanochains. Inset is the enlarged view of hysteresis loop.

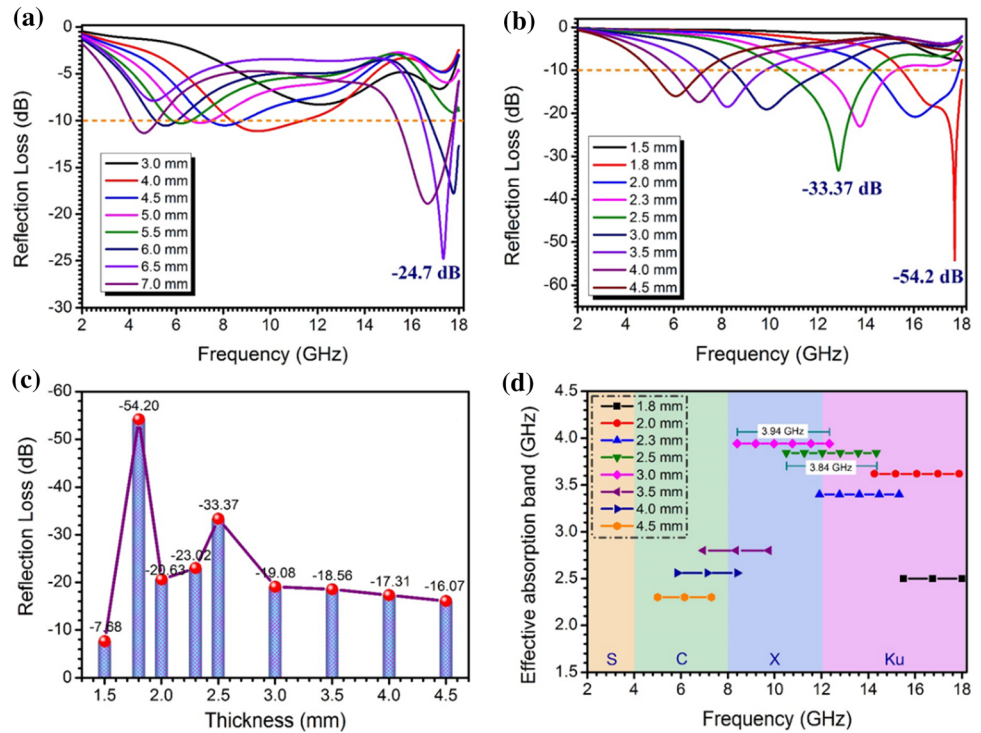
whereas the difference in the remanent magnetism may be related to the ferromagnetic property [36].

Microwave absorption behaviors of two different nanochains were investigated in the frequency range of 2–18 GHz at room temperature. Their reflection loss curves are shown in Fig. 9. In order to be

convenient to distinguish these two samples,  $\text{Fe}_3\text{O}_4@\text{void}@\text{SiO}_2$  nanochains and  $\text{Fe}_3\text{O}_4@\text{void}@\text{SiO}_2@\text{PPy}$  nanochains will be renamed as FVS nanochains and FVSP nanochains, respectively. From Fig. 9a, one can obviously see three sharp peaks in the high-frequency region. The peak values are  $-17.7$  dB (17.76 GHz),  $-24.7$  dB (17.34 GHz),  $-18.96$  dB (16.69 GHz) at the layer thickness of 6.0, 6.5 and 7.0 mm, respectively. Meanwhile, it can be found that the largest effective absorption bandwidth is 2.41 GHz (15.40–17.81 GHz) at the layer thickness of 7.0 mm. The results reflect the microwave absorption capacity of FVS nanochains. Compared with the FVS nanochains, FVSP nanochains exhibit superior microwave absorption performance, which can be demonstrated by the reflection loss curves in Fig. 9b. The minimum reflection loss ( $\text{RL}_{\min}$ ) value reaches to  $-54.2$  dB (17.70 GHz) at the layer thickness of 1.8 mm. When the layer thickness is adjusted to 2.5 mm, the  $\text{RL}_{\min}$  value is  $-33.37$  dB (12.86 GHz). Moreover, Fig. 9c shows series of the  $\text{RL}_{\min}$  values of FVSP nanochains at different layer thicknesses. One can find that majority of the  $\text{RL}_{\min}$  values are below  $-15.0$  dB, and at the layer thickness of 1.8–2.5 mm

**Figure 9** Reflection loss curves of paraffin-based composites containing 20 wt% nanochains:

**a**  $\text{Fe}_3\text{O}_4@\text{void}@\text{SiO}_2$  and **b**  $\text{Fe}_3\text{O}_4@\text{void}@\text{SiO}_2@\text{PPy}$ . **c** Column chart of the minimum reflection loss values of  $\text{Fe}_3\text{O}_4@\text{void}@\text{SiO}_2@\text{PPy}$  nanochains at different layer thicknesses; **d** effective absorption bandwidth of  $\text{Fe}_3\text{O}_4@\text{void}@\text{SiO}_2@\text{PPy}$  nanochains at different layer thicknesses.



the  $RL_{\min}$  values are even under  $-20.0$  dB, indicating the excellent microwave absorption capacity. In addition, the variation trend of  $RL_{\min}$  values is also depicted in Fig. 9c. The  $RL_{\min}$  values gradually increase with the layer thickness ranging from 2.5 mm to 4.5 mm. Figure 9d shows the effective absorption band of FVSP nanochains at different layer thicknesses. The largest effective absorption bandwidth reaches to 3.94 GHz in the frequency range of 8.4–12.34 GHz, which almost covers the whole X band. When the layer thickness is adjusted to 2.5 mm, the absorption band is about 3.84 GHz, which is also larger than 2.41 GHz of FVS nanochains. Through the detailed comparison between two samples in the two aspect of absorption capacity and effective absorption bandwidth, it can be confirmed that FVSP nanochains possess stronger microwave absorption performance than FVS nanochains. Besides, FVSP nanochains are with much thinner layer thicknesses than FVS nanochains. Therefore, FVSP nanochains will be considered as more promising candidates in the practical application of microwave absorption than FVS nanochains.

To reveal the microwave absorption mechanisms of nanochains, the related electromagnetic parameters are investigated. As is known, the real permittivity ( $\epsilon'$ ) and the real permeability ( $\mu'$ ) represent the

storage ability of electric and magnetic energy, while the imaginary permittivity ( $\epsilon''$ ) and the imaginary permeability ( $\mu''$ ) stand for the electric energy dissipation and magnetic loss, respectively. From Fig. 10a, one can see that the  $\epsilon'$  values of FVSP nanochains are bigger than that of FVS nanochains in the whole frequency band, demonstrating the stronger storage ability and happening more polarizations. In the frequency range of 2–13 GHz, the  $\epsilon'$  values gradually decrease with the increasing of frequency. This is because some polarizations don't catch up with the periodical change of electromagnetic wave [37]. In the rest of frequency band, the  $\epsilon'$  values of FVSP nanochains have sharp fluctuations in the range of 6.6–7.4 while that of FVS nanochains have slight fluctuations around 3.1. This result denotes the occurrence of resonance behavior in the high-frequency band. From Fig. 10b and c, one can find that the  $\epsilon''$  values of FVSP nanochains first increase from 3.89 to 4.14 in the 2–4.4 GHz, gradually decrease from 4.14 to 2.98 in the 4.4–14.3 GHz, then have a wide peak in the 14.3–18.0 GHz. The  $\epsilon''$  values of FVS nanochains are 1.1–1.2 in the 2.0–11.5 GHz, then have a sharp decrease from 1.2 to 0.66 in the 11.5–15.7 GHz and appear a slight fluctuation of 0.66–0.77 in the rest frequency band. According to the fluctuant dielectric spectra of imaginary permittivity in the 14–18 GHz,



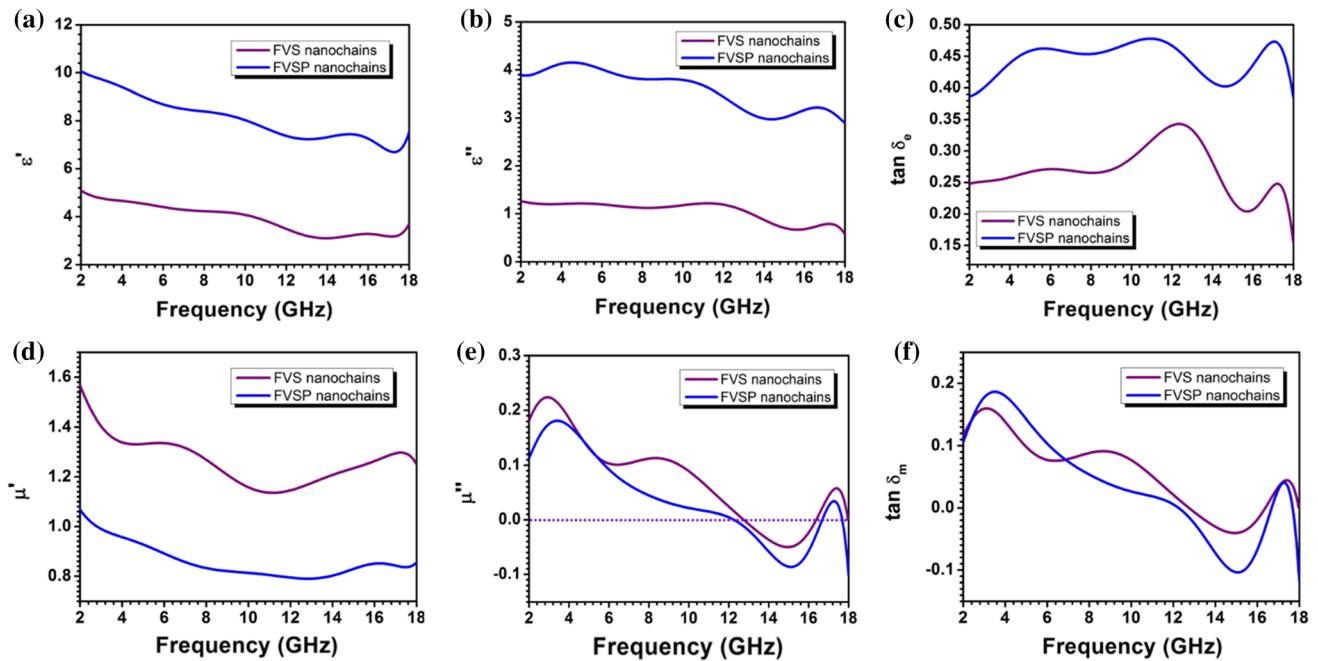


**Figure 10** Electromagnetic parameters of two nanochains: **a** real parts and **b** imaginary parts of permittivity, **c**  $\tan \delta_e$  values, **d** real parts and **e** imaginary parts of permeability, **f**  $\tan \delta_m$  values.

one can see several broad peaks, indicating the generation of dielectric resonance loss. Moreover, the comparison of two  $\epsilon''$  curves demonstrates that FVSP nanochains possess higher dielectric loss than FVS nanochains, which can also be verified by the dielectric loss tangent ( $\tan \delta_e = \epsilon''/\epsilon'$ ) curves in Fig. 10c. Complex permeability of nanochains has a significant influence on the microwave absorption performance. From Fig. 10d, one can find that the  $\mu'$  values of FVS nanochains are much higher than that of FVSP nanochains over the whole frequency range, which may be ascribed to the stronger saturation magnetization. Figure 10e shows the  $\mu''$  curves of FVS and FVSP nanochains. The  $\mu''$  values of FVSP nanochains first increase from 0.11 to 0.18 in the 2–3.37 GHz, decrease from 0.18 to  $-0.087$  in the 3.37–15.15 GHz, then rapidly raise from  $-0.087$  to 0.035 in the 15.15–17.3 GHz and again decrease from 0.035 to  $-0.098$  in the rest frequency band. The  $\mu''$  values of FVS nanochains have an increase from 0.18 to 0.22 in the 2–2.86 GHz and a sharp decrease from 0.22 to 0.10 in the 2.86–6.40 GHz, then they keep a tiny fluctuation of 0.10–0.11 in the 6.40–8.50 GHz, rapidly decline from 0.11 to  $-0.05$  in the 8.50–15.0 GHz, again increase from  $-0.05$  to 0.06 in the 15.0–17.36 GHz and decrease from 0.06 to 0.0 in the 17.36–18.0 GHz. It can be found that the  $\mu''$  values of FVS nanochains

are higher than that FVSP nanochains, indicating larger magnetic loss. Additionally, the magnetic loss tangent ( $\tan \delta_m = \mu''/\mu'$ ) curves in Fig. 10f demonstrate FVS nanochains exhibit stronger magnetic loss than FVSP nanochains in the 6.8–18.0 GHz. However, the  $\tan \delta_m$  values of FVSP nanochains are less than 0.2 while the  $\tan \delta_e$  values are greater than 0.2. This result indicates that the dielectric loss has functioned as a primary role in the electromagnetic energy dissipation for FVSP nanochains.

Generally speaking, dielectric loss originates from the conductive loss, interfacial polarization, ionic polarization, electronic polarization, dipole polarization and dielectric relaxation [38]. The electronic polarization usually occurs in the ultraviolet frequency range ( $10^{14}$ – $10^{16}$  Hz), and ionic polarization is often located in the  $10^{11}$ – $10^{13}$  Hz, so these two polarizations have few contributions to dielectric loss in the 2–18 GHz [39]. The formation of three-dimensional (3D) conductive networks assembled by numerous FVSP nanochains is conducive to the aggregation of numerous electrons, which can induce the generation of microcurrent in the networks [24, 40]. Moreover, one-dimensional (1D) structured orientation can accelerate the flow of electrons, facilitating to raise the microcurrent and leading to high conductive loss. This is because of the existence

of conductive PPy shells with the doping degree of 23.53%. On the contrary, the FVS nanochains have no conductive loss in the whole frequency range, for SiO<sub>2</sub> shells are insulation. Factually, the dipoles of Fe<sup>2+</sup>–O–Fe<sup>3+</sup> in the alternating electromagnetic field can producing the dipole polarizations in the both nanochains. The PPy and p-TSA dopants can be regarded as extra dipoles in the FVSP nanochains, which can further promote the electromagnetic energy dissipation. It is known that interfacial polarizations are important in the enhancement of dielectric loss. According to the yolk–shell structure, FVS nanochains mainly involve three kinds of interfacial polarizations, such as between Fe<sub>3</sub>O<sub>4</sub> cores and SiO<sub>2</sub> shells, Fe<sub>3</sub>O<sub>4</sub> cores and air/paraffin, SiO<sub>2</sub> shells and air/paraffin. For the FVSP nanochains, the interfacial polarizations have occurred on different interfaces, including between Fe<sub>3</sub>O<sub>4</sub> cores and air/paraffin, Fe<sub>3</sub>O<sub>4</sub> cores and SiO<sub>2</sub> shells, SiO<sub>2</sub> shells and PPy shells, SiO<sub>2</sub> shells and air, PPy shells and paraffin. Besides, relaxation loss is another factor contributing to the dielectric loss. The typical relaxation loss is Debye dielectric relaxation, which can be expressed by a Cole–Cole semicircle [41, 42]. Based on the Debye relaxation equation, the relationship between ε' and ε'' can be deduced as follow:

$$\left(\epsilon' - \frac{\epsilon_s + \epsilon}{2}\right)^2 + (\epsilon'')^2 = \left(\frac{\epsilon_s - \epsilon}{2}\right)^2 \tag{3}$$

ε<sub>s</sub> is the static permittivity and ε is the relative dielectric permittivity at the high-frequency limit. It can be inferred that the curve of ε'' versus ε' will be consisted of several semicircle, and a single semicircle is usually denoted as a Cole–Cole semicircle, indicating a Debye relaxation process. Figure 11a and b shows the Cole–Cole plots of FVS and FVSP nanochains, respectively. One can clearly see that there are two semicircles (marked as ❷ and ❸) in the FVS nanochains, so are FVSP nanochains (marked as ❸ and ❹), demonstrating the occurrence of Debye relaxation. And the rest curves are irregular semicircles in the both nanochains, which may be ascribed to the Maxwell–Wagner relaxations [43]. On the basis of the above discussion, it can be concluded that the dielectric loss of FVS nanochains mainly originate from the interfacial polarizations, dipole polarizations, Debye relaxations and Maxwell–Wagner relaxations. With the introduction of PPy shells, the nanochains not only produce high conductive loss, extra dipole polarizations and more interfacial

polarizations but also maintain the Debye relaxations and Maxwell–Wagner relaxations loss. In addition, the magnetic loss mechanism has also been revealed. The appearance of negative μ'' values in Fig. 10e demonstrates that magnetic energy has been radiated out from the nanochains [44]. The absorption peaks of μ'' values in the high frequency band stem from the domain wall resonance and natural resonance, which can also be evidenced by the magnetic loss tangent curves [45, 46]. Furthermore, the natural resonance effect can be described by the following equation:

$$2\pi f_r = rH_x \tag{4}$$

$$H_x = 4|K_1|/3\mu_0 M_s \tag{5}$$

$$K_1 = \mu_0 M_s H_c / 2 \tag{6}$$

where μ<sub>0</sub> is the universal value of permeability in free space (4π × 10<sup>-7</sup> H/m), *r* is the gyromagnetic ratio, *H<sub>x</sub>* is the anisotropy energy, |*K<sub>1</sub>*| is the anisotropy coefficient, *M<sub>s</sub>* and *H<sub>c</sub>* represent the saturation magnetization and coercivity. It can be inferred that the resonance frequency depends on the effective anisotropy field, which is associated with the coercivity values of the materials. The hysteresis loops show that FVS and FVSP nanochains have the same coercivity, which can explain their similar resonance frequency depicted in Fig. 10e. This result indicates the natural resonance play a primary role in the resonance loss. In addition, the eddy current loss has been considered and expressed by the following eddy equation [47]:

$$C_0 = \mu''(\mu')^{-2} f^{-1} = 2\pi\mu_0 d^2 \delta \tag{7}$$

If the eddy current effect is present in the microwave absorption, the *C<sub>0</sub>* values will keep constant with changing the frequency. Figure 11c shows the *C<sub>0</sub>* curves of FVS and FVSP nanochains. One can just see a platform in the *C<sub>0</sub>* curve of FVS nanochains, indicating the existence of eddy current loss. Through the above mentioned analysis, it can be confirmed that the magnetic loss of FVS nanochains stems from the domain wall resonance, natural resonance and eddy current loss, while that of FVSP nanochains is mainly derived from the domain wall resonance and natural resonance.

Impedance matching is also an important factor in the microwave absorption application, which can be expressed by the relative input impedance |*Z<sub>in</sub>*/*Z<sub>0</sub>*| [48, 49]. The values of |*Z<sub>in</sub>*/*Z<sub>0</sub>*| are close to 1, denoting

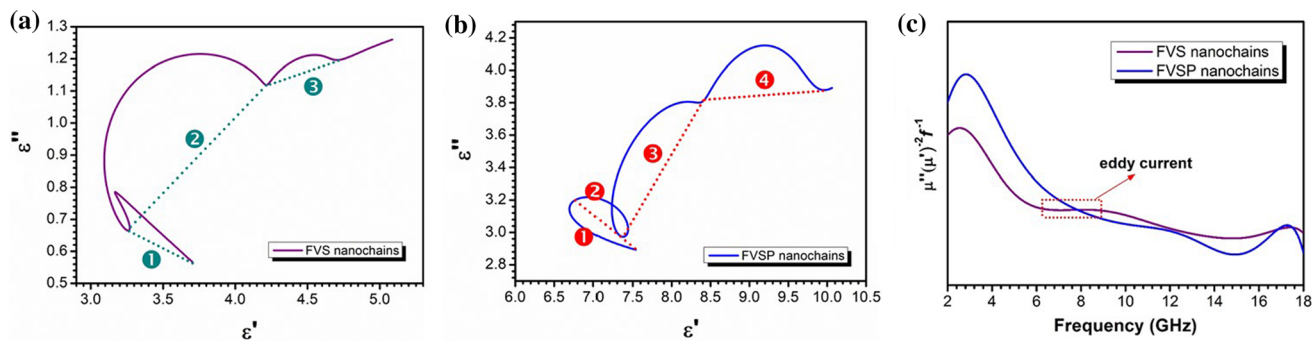


**Figure 11** Cole–Cole plots of **a** FVS and **b** FVSP nanochains, and **c**  $C_0$  values of FVS and FVSP nanochains.

the good impedance matching. From the counter maps in Fig. 12a, one can see the boundary line (equal to 1) between yellow and green areas crosses the whole frequency range with the variation of layer thicknesses for FVS nanochains. As shown in Fig. 12b, the boundary line (equal to 1) between blue and purple areas crosses two frequency bands of 12.60–16.70 GHz and 17.60–18.0 GHz. It can be inferred that the FVS nanochains have the better impedance matching than FVSP nanochains, which can also be evidenced by the closer distance of  $\tan\delta_e$  and  $\tan\delta_m$  values from Fig. 10c and f. Moreover, one can also find that the two peaks of reflection loss values for FVSP nanochains are exactly located in the 12.60–16.70 GHz and 17.60–18.0 GHz range, respectively. This result demonstrates impedance matching has a great contribution to enhancing the microwave absorption performance. In addition, numerous pores and large number of spaces can induce the multiple reflection and absorption of electromagnetic waves in the yolk–shell nanochains. To further evaluate the dissipation ability of microwave absorbing materials, the attenuation constant  $\alpha$  values have been considered and expressed by the following equation:

$$\alpha = \frac{\sqrt{2}\pi f}{c} \times \sqrt{(\mu''\varepsilon'' - \mu'\varepsilon') + \sqrt{(\mu''\varepsilon'' - \mu'\varepsilon')^2 + (\mu'\varepsilon'' - \mu''\varepsilon')^2}} \quad (8)$$

where  $c$  and  $f$  represent the velocity of light and frequency, respectively. Figure 12c shows the attenuation constant  $\alpha$  variations of FVS and FVSP nanochains in the frequency range of 2–18 GHz. As is seen clearly, the FVSP nanochains possess the higher  $\alpha$  values than FVS nanochains, indicating the stronger microwave absorption capability.

According to the above discussion, the detailed microwave absorption mechanism of FVSP nanochains has been revealed. Firstly, excellent impedance matching promotes more electromagnetic wave intruding into the materials, benefiting to strengthening the interaction between electromagnetic wave and absorption materials. Secondly, the dielectric loss conducts more contribution to the dissipation of electromagnetic wave energy. With the coating of PPy shells, conductive loss, dipole polarizations, interfacial polarizations, multiple reflection and absorption have been added to largely enhance

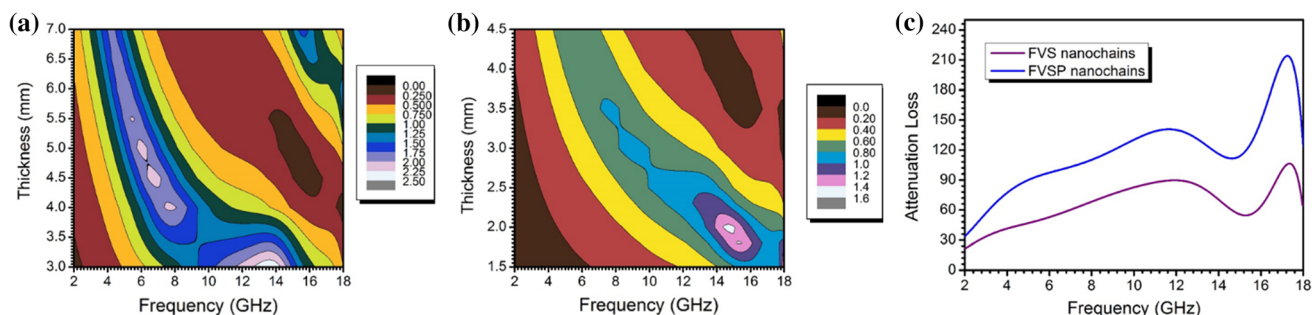


**Figure 12** The counter maps of  $|Z_{in}/Z_0|$  values for **a** FVS and **b** FVSP nanochains, and **c** attenuation constant curves of FVS and FVSP nanochains.

the dielectric loss. Figure 13 shows the detailed dielectric loss mechanism for  $\text{Fe}_3\text{O}_4@\text{void}@\text{SiO}_2@\text{PPy}$  nanochains. Besides, the magnetic loss is also existed, which mainly stems from the domain wall resonance and natural resonance.

The effect of mass fraction of  $\text{Fe}_3\text{O}_4@\text{void}@\text{SiO}_2@\text{PPy}$  nanochains in the paraffin-based composites on microwave absorption properties is investigated. As the percentage increases from 20 to 35 wt% and even 50 wt%, the reflection loss behaviors have some changes. According to Fig. 14a and b, one can see that at different layer thicknesses most of reflection loss peak values always exceed  $-20$  dB (equal to 99% absorption efficiency), and the  $\text{RL}_{\text{min}}$  values are  $-44.62$  dB (13.55 GHz) and  $-45.33$  dB (14.52 GHz), respectively. According to the reflection loss curves, Fig. 14c and d depicts the effective absorption frequency band of composites with floating column and the corresponding bandwidth is also shown. Interestingly, when the mass fraction of nanochains in the composites is adjusted to 35 wt%, several absorption bandwidths are greater than 5.0 GHz and the maximum one can reach 5.9 GHz (11.49–17.39 GHz). Additionally, at the layer thicknesses of 2.9 mm and 4.0 mm, both of broad absorption bands enable to cover the whole X band and Ku band, respectively. With the mass fraction up to 50 wt%, the maximum absorption bandwidth is around 4 GHz, which is close to that of composites containing 20 wt% nanochains. However, it is unusual that their absorption bands at the layer thicknesses of 5.8, 6.0, 6.2, 7.0 and 8.0 mm are divided into two parts, which are located in the low and high frequency range, respectively, satisfying the multiband absorption. The above results indicate that paraffin-based composites

containing  $\text{Fe}_3\text{O}_4@\text{void}@\text{SiO}_2@\text{PPy}$  nanochains can possess the strong absorption capability and broad absorption frequency bandwidth.

In the end, the comparison between sphere-like and chain-like composites as microwave absorbers has been conducted. Both of yolk-shell  $\text{Fe}_3\text{O}_4@\text{void}@\text{SiO}_2$  and  $\text{Fe}_3\text{O}_4@\text{void}@\text{SiO}_2@\text{PPy}$  microspheres have been first prepared, and the detailed preparation process is given in supporting information. Moreover, the microstructure of microspheres was characterized by a transmission electron microscope. According to TEM images in Figure S2, one can clearly see the yolk-shell structure in the  $\text{Fe}_3\text{O}_4@\text{void}@\text{SiO}_2$  and  $\text{Fe}_3\text{O}_4@\text{void}@\text{SiO}_2@\text{PPy}$  microspheres. Subsequently, microwave absorption performance of paraffin-based composites containing 20 wt% microspheres has been investigated, and the resulting reflection loss curves are depicted in Figure S3. It is easily found that the  $\text{RL}_{\text{min}}$  value of  $\text{Fe}_3\text{O}_4@\text{void}@\text{SiO}_2$  microspheres is just over  $-15$  dB, and that of  $\text{Fe}_3\text{O}_4@\text{void}@\text{SiO}_2@\text{PPy}$  microspheres can reach  $-40.15$  dB. This result once again indicates that encapsulation of PPy shells promotes the enhancement of microwave absorption performance for yolk-shell  $\text{Fe}_3\text{O}_4@\text{void}@\text{SiO}_2$  microspheres. It is well known that excellent microwave absorbers need to meet important features of strong absorption capability, broad effective absorption width, low density and lightweight. To further clarify the difference of sphere-like and chain-like composites as microwave absorbers, we conduct the comparison in the aspects of minimum reflection loss value, maximum effective absorbing bandwidth and layer thickness. The relevant data are listed in Table S1. One can find that chain-like composites exhibit

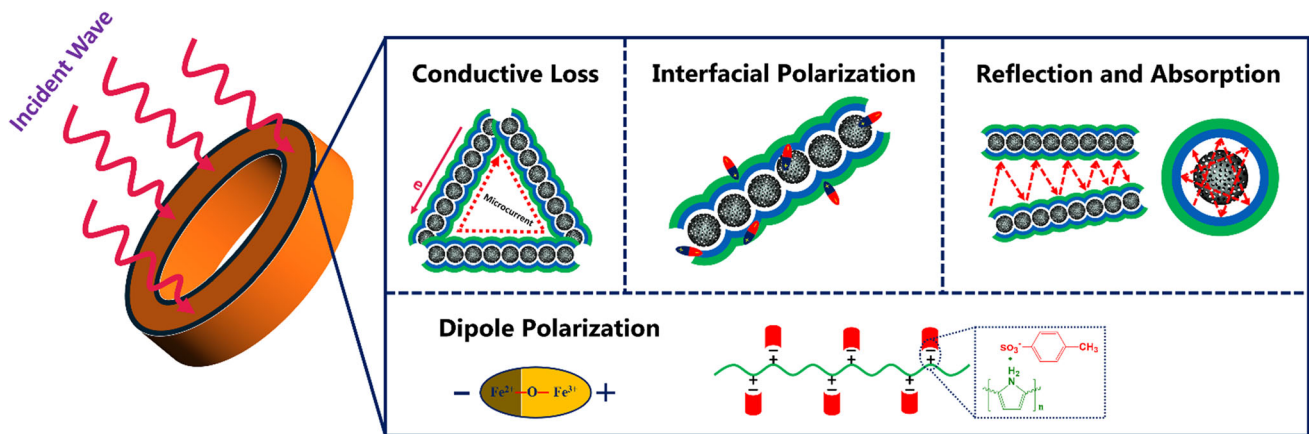


**Figure 13** Dielectric loss mechanism of yolk-shell  $\text{Fe}_3\text{O}_4@\text{void}@\text{SiO}_2@\text{PPy}$  nanochains as microwave absorbers.

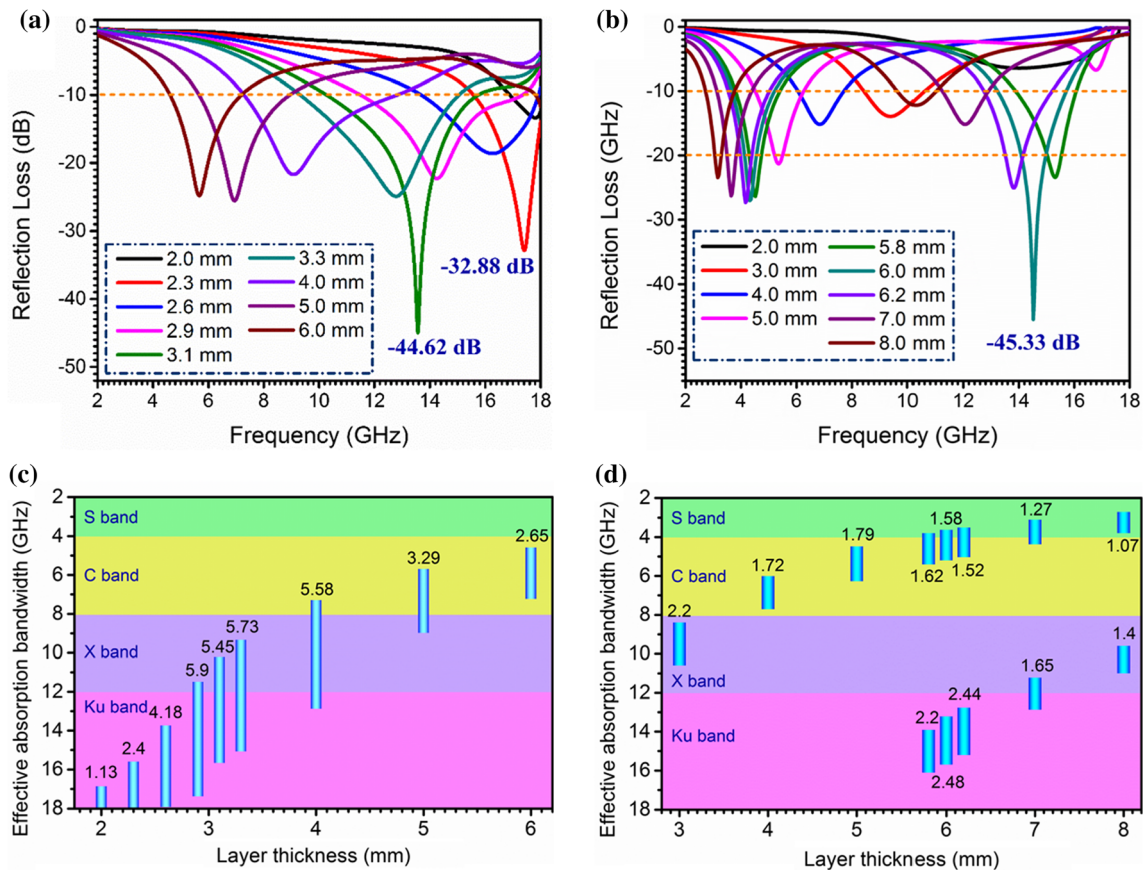


**Figure 14** Reflection loss curves and effective absorption bandwidth for paraffin-based composites containing (a, c) 35 wt% and (b, d) 50 wt%  $\text{Fe}_3\text{O}_4@void@SiO_2@PPy$  nanochains.

smaller  $RL_{min}$  value than sphere-like counterparts, indicating stronger microwave absorption. On the contrary, effective absorption bandwidth of chain-like composites is inferior to that of microspheres. But the layer thickness of  $\text{Fe}_3\text{O}_4@void@SiO_2@PPy$  microspheres is much larger than that of chain-like  $\text{Fe}_3\text{O}_4@void@SiO_2@PPy$  composites, which greatly limits their application fields. Based on above comprehensive analysis, chain-like  $\text{Fe}_3\text{O}_4@void@SiO_2@PPy$  composites will be the most promising candidates as microwave absorbents among the four samples. Besides, tailoring the chain length distribution of  $\text{Fe}_3\text{O}_4@void@SiO_2@PPy$  can further optimize the microwave absorption performance. Therefore, core-shell chain-like composites are more potential in the improvement of microwave absorption performance than corresponding core-shell microspheres.

## Conclusion

In this work, we have first prepared the novel yolk-shell  $\text{Fe}_3\text{O}_4@void@SiO_2$  nanochains via the magnetic-field-induced distillation-precipitation polymerization together with sacrificial template processes. Then,  $\text{Fe}_3\text{O}_4@void@SiO_2$  nanochains have been coated by PPy shells through a facile chemical oxidative polymerization. The lengths of nanochains are mainly distributed in the 10–15  $\mu\text{m}$ , exhibiting high aspect ratio. The yolk-shell structure endows nanochains with good porosity.  $\text{Fe}_3\text{O}_4@void@SiO_2$  nanochains and  $\text{Fe}_3\text{O}_4@void@SiO_2@PPy$  nanochains have the BET specific surface area of 49  $\text{m}^2/\text{g}$  and 42  $\text{m}^2/\text{g}$ , respectively. Investigations of microwave absorbing properties indicate that  $\text{Fe}_3\text{O}_4@void@SiO_2@PPy$  nanochains have stronger absorption capability and broader effective absorption bandwidth than  $\text{Fe}_3\text{O}_4@void@SiO_2$  nanochains. The minimum reflection loss value is  $-54.2$  dB (17.70 GHz) and effective absorption frequency

bandwidth can reach 5.9 GHz (11.49–17.39 GHz), so they will become promising candidates in the application of microwave absorption. The analysis of microwave absorption mechanism reveals that introduction of PPy shells can increase the conductive loss, dipole polarizations, interfacial polarizations, multiple reflection and absorption among network-like nanochains. This discovery presents a new platform for further studies of core–shell structured composites as microwave absorbing materials.

## Acknowledgements

The authors are grateful for the financial support provided by the Foundation of National Natural Science Foundation of China (No. 51433008), National Science Foundation for Young Scientists of China (Grant No. 51503116) and Fundamental Research Funds for the Central Universities (No. 3102017jc01001). The authors thank the Analytical & Testing Center of Northwestern Polytechnical University for the SEM and TEM test.

## Funding

The authors declare no competing financial interest.

**Electronic supplementary material:** The online version of this article (<https://doi.org/10.1007/s10853-020-05313-y>) contains supplementary material, which is available to authorized users.

## References

- [1] Shahzad F, Alhabeab M, Hatter CB, Anasori B, Man HS, Koo CM, Gogotsi Y (2016) Electromagnetic interference shielding with 2D transition metal carbides (MXenes). *Science* 353(6304):1137–1140
- [2] Herzer G (1996) Nanocrystalline soft magnetic materials. *J Magn Magn Mater* 157–158(5):133–136
- [3] Chen ZP, Xu C, Ma CQ, Ren WC, Cheng HM (2013) Lightweight and flexible graphene foam composites for high-performance electromagnetic interference shielding. *Adv Mater* 25(9):1296–1300
- [4] Wang GZ, Gao Z, Tang SW, Chen CQ, Duan FF, Zhao SC, Lin SW, Feng YH, Zhou L, Qin Y (2012) Microwave absorption properties of carbon nanocoils coated with highly controlled magnetic materials by atomic layer deposition. *ACS Nano* 6(12):11009–11017
- [5] Watts CM, Liu XL, Padilla WJ (2012) Metamaterial electromagnetic wave absorbers. *Adv Mater* 24(23):OP98–OP120
- [6] You WB, Bi H, She W, Zhang Y, Che RC (2017) Dipolar-distribution cavity  $\gamma$ -Fe<sub>2</sub>O<sub>3</sub>@C@ $\alpha$ -MnO<sub>2</sub> nanospindle with broadened microwave absorption bandwidth by chemically etching. *Small* 13(5):1602779
- [7] Zhang HX, Jia ZR, Feng AL, Zhou ZH, Chen L, Zhang CH, Liu XH, Wu GL (2020) In situ deposition of pitaya-like Fe<sub>3</sub>O<sub>4</sub>@C magnetic microspheres on reduced graphene oxide nanosheets for electromagnetic wave absorber. *Compos Part B* 199:108261
- [8] Liu QH, Cao Q, Bi H, Liang CY, Yuan KP, She W, Yang YJ, Che RC (2016) CoNi@SiO<sub>2</sub>@TiO<sub>2</sub> and CoNi@Air@TiO<sub>2</sub> microspheres with strong wideband microwave absorption. *Adv Mater* 28(3):486–490
- [9] Chen C, Liu QH, Bi H, You WB, She W, Che RC (2016) Fabrication of hierarchical TiO<sub>2</sub> coated Co<sub>20</sub>Ni<sub>80</sub> particles with tunable core sizes as high-performance wide-band microwave absorbers. *Phys Chem Chem Phys* 18(38):26712–26718
- [10] Chen YJ, Gao P, Wang RX, Zhu CL, Wang LJ, Cao MS, Jin HB (2009) Porous Fe<sub>3</sub>O<sub>4</sub>/SnO<sub>2</sub> core/shell nanorods: synthesis and electromagnetic properties. *J Phys Chem C* 113(23):10061–10064
- [11] Du YC, Liu WW, Qiang R, Wang Y, Han XJ, Ma J, Xu P (2014) Shell thickness-dependent microwave absorption of core–shell Fe<sub>3</sub>O<sub>4</sub>@C composites. *ACS Appl Mater Inter* 6(15):12997–13006
- [12] Liu JW, Che RC, Chen HJ, Zhang F, Xia F, Wu QS, Wang M (2012) Microwave absorption enhancement of multifunctional composite microspheres with spinel Fe<sub>3</sub>O<sub>4</sub> cores and anatase TiO<sub>2</sub> shells. *Small* 8(8):1214–1221
- [13] Zhao B, Guo XQ, Zhao WY, Deng JS, Shao G, Fan BB, Bai ZY, Zhang R (2016) Yolk–shell Ni@SnO<sub>2</sub> composites with a designable interspace to improve the electromagnetic wave absorption properties. *ACS Appl Mater Inter* 8(42):28917–28925
- [14] Zhao B, Shao G, Fan BB, Zhao WY, Zhang R (2015) Investigation of the electromagnetic absorption properties of Ni@TiO<sub>2</sub> and Ni@SiO<sub>2</sub> composite microspheres with core–shell structure. *Phys Chem Chem Phys* 17(4):2531–2539
- [15] Ding D, Wang Y, Li XD, Qiang R, Xu P, Chu WL, Han XJ, Du YC (2017) Rational design of core-shell Co@C microspheres for high-performance microwave absorption. *Carbon* 111:722–732
- [16] Zhou WC, Hu XJ, Bai XX, Zhou SY, Sun CH, Yan J, Chen P (2011) Synthesis and electromagnetic, microwave absorbing

- properties of core-shell  $\text{Fe}_3\text{O}_4$ -poly (3, 4-ethylenedioxythiophene) microspheres. *ACS Appl Mater Inter* 3(10):3839–3845
- [17] Feng JT, Hou YH, Wang YC, Li LC (2017) Synthesis of hierarchical  $\text{ZnFe}_2\text{O}_4@/\text{SiO}_2@/\text{RGO}$  core-shell microspheres for enhanced electromagnetic wave absorption. *ACS Appl Mater Inter* 9(16):14103–14111
- [18] Han R, Li W, Pan WW, Zhu MG, Zhou D, Li FS (2014) 1D Magnetic materials of  $\text{Fe}_3\text{O}_4$  and Fe with high performance of microwave absorption fabricated by electrospinning method. *Sci Rep* 4(1):7493
- [19] Zhang XF, Li YX, Liu RG, Rao Y, Rong HW, Qin GW (2016) High-magnetization FeCo nanochains with ultrathin interfacial gaps for broadband electromagnetic wave absorption at gigahertz. *ACS Appl Mater Inter* 8(5):3494–3498
- [20] Hou Y, Cheng LF, Zhang YN, Yang Y, Deng CR, Yang ZH, Chen Q, Wang P, Zheng LX (2017) Electrospinning of Fe/SiC hybrid fibers for highly efficient microwave absorption. *ACS Appl Mater Inter* 9(8):7265–7271
- [21] Li N, Huang GW, Li YQ, Xiao HM, Feng QP, Hu N, Fu SY (2017) Enhanced microwave absorption performance of coated carbon nanotubes by optimizing the  $\text{Fe}_3\text{O}_4$  nanocoating structure. *ACS Appl Mater Inter* 9(3):2973–2983
- [22] Kong LB, Li ZW, Liu L, Huang R, Abshinova M, Yang ZH, Tang CB, Tan PK, Deng CR, Matitsine S (2013) Recent progress in some composite materials and structures for specific electromagnetic applications. *Int Mater Rev* 58(4):203–259
- [23] Chiu SC, Yu HC, Li YY (2010) High electromagnetic wave absorption performance of silicon carbide nanowires in the gigahertz range. *J Phys Chem C* 114(4):1947–1952
- [24] Liu J, Cao MS, Luo Q, Shi HL, Wang WZ, Yuan J (2016) Electromagnetic property and tunable microwave absorption of 3D nets from nickel chains at elevated temperature. *ACS Appl Mater Inter* 8(34):22615–22622
- [25] Qiao MT, Lei XF, Ma Y, Tian LD, He XW, Su KH, Zhang QY (2017) Application of yolk-shell  $\text{Fe}_3\text{O}_4@/\text{N}$ -doped carbon nanochains as highly effective microwave-absorption material. *Nano Res* 11(3):1500–1519
- [26] Ma ML, Li WT, Tong ZY, Yang YY, Ma Y, Cui ZH, Wang RZ, Lu P, Huang WB (2020) 1D flower-like  $\text{Fe}_3\text{O}_4@/\text{SiO}_2@/\text{MnO}_2$  nanochains inducing RGO self-assembly into aerogels for high-efficient microwave absorption. *Mater Des* 188:108462
- [27] Guo J, Song HX, Liu H, Luo CJ, Ren YR, Ding T, Khan MA, Young DP, Liu XY, Zhang X, Kong J, Guo ZH (2017) Polypyrrole-interface-functionalized nano-magnetite epoxy nanocomposites as electromagnetic wave absorbers with enhanced flame retardancy. *J Mater Chem C* 5:5334–5344
- [28] Liu YL, Li CM, Zhang HT, Fan XL, Liu Y, Zhang QY (2015) One-pot hydrothermal synthesis of highly monodisperse water-dispersible hollow magnetic microspheres and construction of photonic crystals. *Chem Eng J* 259:779–786
- [29] Ma ML, Zhang QY, Dou JB, Zhang HP, Yin DZ, Geng WC, Zhou YY (2012) Fabrication of one-dimensional  $\text{Fe}_3\text{O}_4/\text{P}$  (GMA–DVB) nanochains by magnetic-field-induced precipitation polymerization. *J Colloid Interf Sci* 374(1):339–344
- [30] Ma ML, Zhang QY, Dou JB, Zhang HP, Yin DZ, Chen SJ (2012) Fabrication of 1D  $\text{Fe}_3\text{O}_4/\text{P}$ (NIPAM–MBA) thermosensitive nanochains by magnetic-field-induced precipitation polymerization. *Colloid Polym Sci* 290(12):1207–1213
- [31] Qiao MT, Lei XF, Ma Y, Tian LD, Su KH, Zhang QY (2016) Well-defined core-shell  $\text{Fe}_3\text{O}_4@/\text{polypyrrole}$  composite microspheres with tunable shell thickness: synthesis and their superior microwave absorption performance in the Ku band. *Ind Eng Chem Res* 55(22):6263–6275
- [32] Yang M, Ma J, Niu Z, Dong X, Xu H, Meng Z, Jin Z, Lu Y, Hu Z, Yang Z (2005) Synthesis of spheres with complex structures using hollow latex cages as templates. *Adv Funct Mater* 15(9):1523–1528
- [33] Li GL, Liu G, Kang ET, Neoh KG, Yang X (2008) pH-responsive hollow polymeric microspheres and concentric hollow silica microspheres from silica-polymer core-shell microspheres. *Langmuir* 24(16):9050–9055
- [34] Li GL, Kang ET, Neoh KG, Yang X (2009) Concentric hollow nanospheres of mesoporous silica shell-titania core from combined inorganic and polymer syntheses. *Langmuir* 25(8):4361–4364
- [35] Qiao MT, Lei XF, Ma Y, Tian LD, Wang WB, Su KH, Zhang QY (2017) Facile synthesis and enhanced electromagnetic microwave absorption performance for porous core-shell  $\text{Fe}_3\text{O}_4@/\text{MnO}_2$  composite microspheres with lightweight feature. *J Alloy Compd* 693:432–439
- [36] Liu W, Tan SJ, Yang ZH, Ji GB (2018) Enhanced low-frequency electromagnetic properties of MOF-derived cobalt through interface design. *ACS Appl Mater Inter* 10(37):31610–31622
- [37] Zhao B, Song Q, Liu W, Sun Y (2014) Overview of dual-active-bridge isolated bidirectional DC–DC converter for high-frequency-link power-conversion system. *IEEE T Power Electr* 29(8):4091–4106
- [38] Ma F, Qin Y, Li YZ (2010) Enhanced microwave performance of cobalt nanoflakes with strong shape anisotropy. *Appl Phys Lett* 96(20):3262

- [39] Zhao B, Zhao WY, Shao G, Fan BB, Zhang R (2015) Morphology-control synthesis of a core-shell structured NiCu alloy with tunable electromagnetic-wave absorption capabilities. *ACS Appl Mater Inter* 7(23):12951–12960
- [40] Fleming J, Koman R (1998) *Web navigation: designing the user experience*. O'reilly Sebastopol, CA
- [41] Zhou XF, Jia ZR, Feng AL, Wang KK, Liu XH, Chen L, Cao HJ, Wu GL (2020) Dependency of tunable electromagnetic wave absorption performance on morphology-controlled 3D porous carbon fabricated by biomass. *Compos Commun* 21:100404
- [42] Xu W, Pan YF, Wei W, Wang GS (2018) Nanocomposites of oriented nickel chains with tunable magnetic properties for high-performance broadband microwave absorption. *ACS Appl Mater Inter* 1(3):1116–1123
- [43] He S, Wang GS, Lu C, Liu J, Wen B, Liu H, Guo L, Cao MS (2013) Enhanced wave absorption of nanocomposites based on the synthesized complex symmetrical CuS nanostructure and poly(vinylidene fluoride). *J Mater Chem A* 1(15):4685–4692
- [44] Zhang WL, Jiang D, Wang X, Hao BN, Liu YD, Liu J (2017) Growth of polyaniline nanoneedles on MoS<sub>2</sub> nanosheets, tunable electro-response and electromagnetic wave attenuation analysis. *J Phys Chem C* 121(9):4989–4998
- [45] Song NN, Yang HT, Liu HL, Ren X, Ding HF, Zhang XQ, Cheng ZH (2013) Exceeding natural resonance frequency limit of monodisperse Fe<sub>3</sub>O<sub>4</sub> nanoparticles via superparamagnetic relaxation. *Sci Rep* 3(1):3161
- [46] Lv HL, Ji GB, Liu W, Zhang HQ, Du YW (2015) Achieving hierarchical hollow carbon@Fe@Fe<sub>3</sub>O<sub>4</sub> nanospheres with superior microwave absorption properties and lightweight feature. *J Mater Chem C* 3(39):10232–10241
- [47] Lv HL, Zhang HQ, Zhao J, Ji GB, Du YW (2016) Achieving excellent bandwidth absorption by a mirror growth process of magnetic porous polyhedron structures. *Nano Res* 9(6):1813–1822
- [48] Zhou XF, Jia ZR, Feng AL, Qu SL, Wang XA, Liu XH, Wang BB, Wu GL (2020) Synthesis of porous carbon embedded with NiCo/CoNiO<sub>2</sub> hybrids composites for excellent electromagnetic wave absorption performance. *J Colloid Interf Sci* 575:130–139
- [49] Tian CH, Du YC, Xu P, Qiang R, Wang Y, Ding D, Xue JL, Ma J, Zhao HT, Han XJ (2015) Constructing uniform core-shell PPy@PANI composites with tunable shell thickness toward enhancement in microwave absorption. *ACS Appl Mater Inter* 7(36):20090–20099

**Publisher's Note** Springer Nature remains neutral with regard to jurisdictional claims in published maps and institutional affiliations.